analytical chemistry

pubs.acs.org/ac Article

Designing Hierarchically Porous Single Atoms of Fe-N_5 Catalytic Sites with High Oxidase-like Activity for Sensitive Detection of Organophosphorus Pesticides

Tiantian Chen, Dandan Zhou, Shenghuai Hou, Yan Li, Ying Liu, Manlin Zhang, Ganbing Zhang,* and Hui Xu*

Cite This: *Anal. Chem.* 2022, 94, 15270−15279 Read Online

ACCESS | Metrics & More | Article Recommendations | Supporting Information

ABSTRACT: Recently, single-atom catalysts (SACs) have been used to construct biosensors for the determination of organophosphorus pesticides (OPs). However, most nanozymes including SACs are peroxidase-like enzymes and require highly toxic and unstable hydrogen peroxide (H_2O_2) as a co-reactant to generate reactive oxygen species. Inspired by the heme site of cytochrome *c* oxidases (Ccos), the construction of Fe-N_5-coordinated SACs by introducing axial N ligands is expected to bind O_2 to generate active metal−oxygen intermediates. Herein, a SAC with an Fe-N_5 active center confined by hierarchically porous carbon nanoframes (Fe SAs/N_5-pC-4) was prepared by a polymerization−pyrolysis−evaporation−etching strategy, and its underlying enzyme-like mechanism was uncovered through experiments and density functional theory calculations. The 100% metal atom utilization, increased accessible active sites, accelerated mass transfer, excellent hydrophilicity, and an electron-driven mechanism of axial N endow the SAC with enhanced oxidase-like activity. Notably, its catalytic rate constant (0.398 s^{-1}) is 569 times greater than that of the commercial Pt/C catalyst. Similar to the catalytic mechanism of Ccos, O_2 can be converted into reactive oxygen species, avoiding the use of co-reactant H_2O_2 effectively. In addition, based on the inhibitory effect of thiols on the active site of Fe SAs/N_5-pC-4, a biosensor was constructed and applied to the colorimetric analysis of OPs. This provides a facile, cost-effective method for efficient OP screening at sites to help control their contamination.

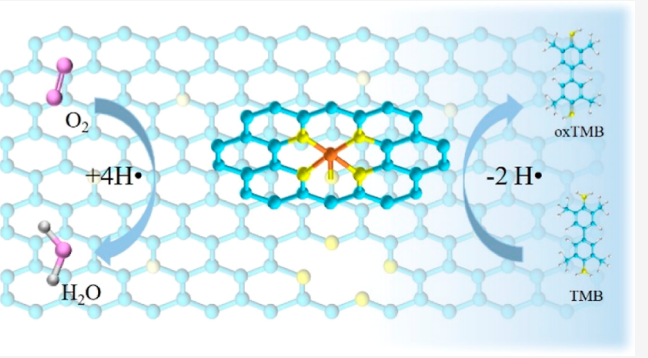

INTRODUCTION

Organophosphorus pesticides (OPs), a class of commonly used pesticides, can destroy cholinesterase and cause cholinergic dysfunction and death.[1] Many traditional methods of detecting OPs such as chromatography-mass spectrometry[2,3] and flow injection analysis[4] exhibit adequate selectivity, sensitivity, and the ability to simultaneous determine multiple analogues. However, the associated high requirements (high cost, multi-steps, specialized instrumentation, etc.) make them unsuitable for environmental monitoring in on-site and resource-limited areas. Compared with the above methods, the colorimetric method possesses the characteristics of simple operation, fast response, low cost, and good selectivity, which has attracted great attention in the field of sensing. For example, colorimetric nanozyme sensor arrays based on heteroatom-doped graphene were fabricated by Wei et al. and successfully used to detect aromatic pesticides.[5] Due to the irreversible inhibition of acetylcholinesterase (AChE) and cholinesterase (BChE) by OPs, recently, biosensors based on the nanozymes and AChE (or BChE) have been developed for high-sensitivity determination of OPs.[6,7]

Nanozymes, a new type of nanomaterials considered as potential substitutes for natural enzymes,[8] have been widely used in the field of analysis recently.[9] Nanozymes solve the problems of high cost and poor stability of natural enzymes and possess unique advantages of tunable catalytic activity, easy large-scale production, and storage.[10] However, suffering from structural complexity and low atom utilization, traditional nanozymes (e.g., transition-metal oxides,[11] noble metals,[12] and carbon nanomaterials[13]) face the problems of low enzyme-like activities, poor catalytic selectivity, and unclear active centers. Given this, it is necessary to further develop nanozymes with precise active sites and high enzymatic activity. Recently, novel single atom catalysts (SACs) in which metal elements are

Received: June 14, 2022
Accepted: October 17, 2022
Published: October 27, 2022

https://doi.org/10.1021/acs.analchem.2c02540
Anal. Chem. 2022, 94, 15270−15279

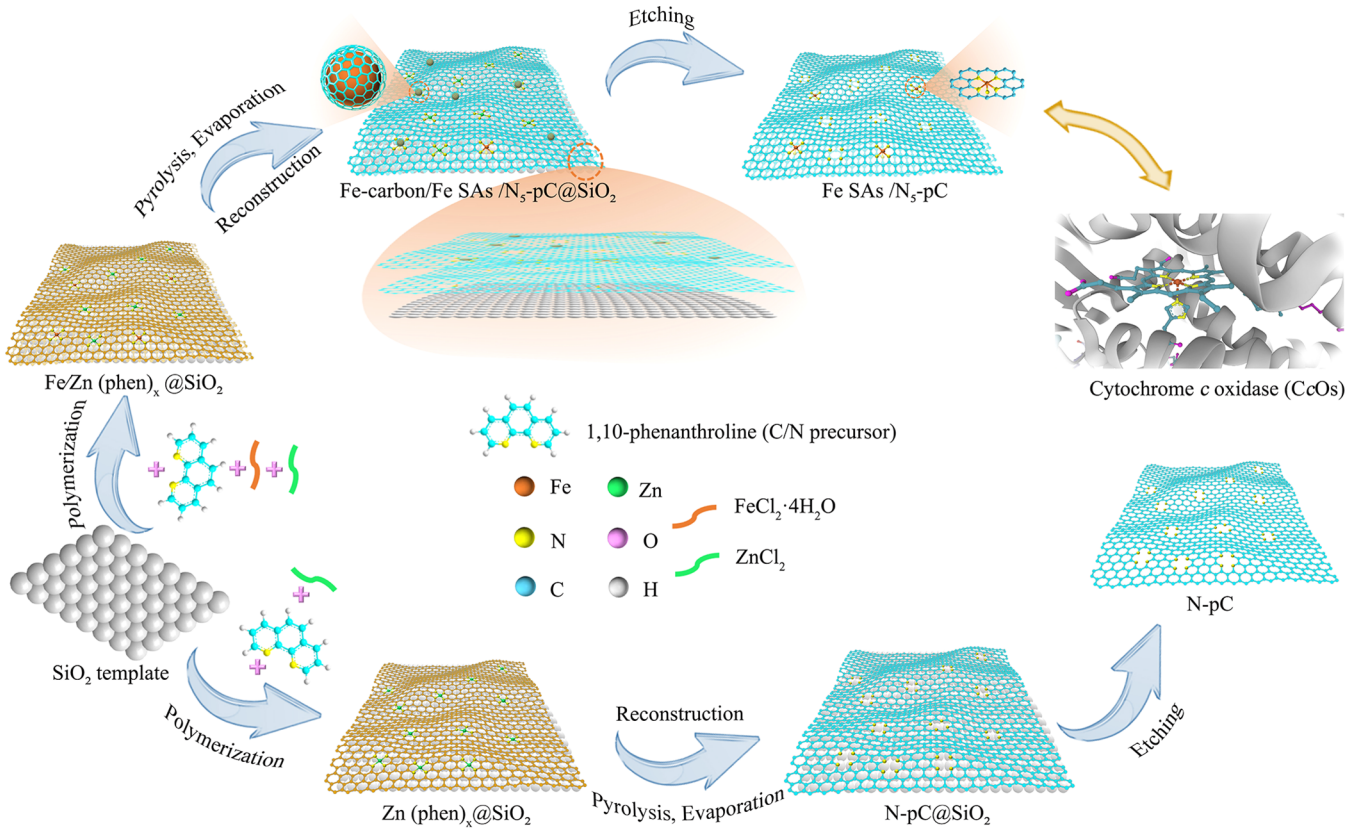

Figure 1. Schematic illustration of the synthesis procedure of Fe SAs/N_5-pC and N-pC.

supported on the surface of solid supports in the form of single atoms have been developed.[14,15] They maximize the utilization of metal atoms and significantly improve the catalytic activity and selectivity compared with traditional nanomaterials.[15] Moreover, unlike traditional nanozymes, the SACs with clear coordination structure information are beneficial to deeply understand the structure−property relationship. However, most of the reported nanozymes including SACs are peroxidase-like enzymes. On this basis, the fabricated target enzyme inhibition sensor adopts H_2O_2 as a co-reactant to generate reactive oxygen species for oxidizing the substrate.[16,17] The instability and high toxicity of H_2O_2 are still the main problems hindering its practical application.[18] Therefore, developing a new class of SACs that generate reactive oxygen species in the absence of H_2O_2 co-reactant is still an urgent need in this field.

To adapt to the aerobic environment, a series of heme proteins have been evolved by nature to activate and reduce O_2.[19] Heme iron can interact with O_2 to give various metal−oxygen intermediates. With the exploration of the catalytic mechanism, researchers found that heme with axial N in cytochrome *c* oxidases (Ccos) can increase the electron density on Fe by donating electrons, namely, the "push effect".[20] It facilitates O_2 binding and enhances the catalytic activity and selectivity.[21] Inspired by this, the construction of Fe-N_5-coordinated SACs by introducing axial N ligands provides a new idea for designing SACs with high oxidase-like properties, and many successful attempts have been made. For example, Huang et al. obtained Fe-N_5-coordinated SACs with oxidase-like activity by pyrolyzing MOF-encapsulated Fe-N_4-coordinated iron phthalocyanines.[22] Hemin was selected by Xu et al. as a precursor of Fe-N_4 sites, which were then assembled on nitrogen-doped graphene to form Fe-N_5 coordinated SACs.[23] The above Fe-N_5-coordinated SACs are mainly obtained by introducing an additional nitrogen source into the Fe-N_4-coordinated species.

Herein, we report a method to design Fe-N_5-coordinated advanced oxidase-like enzymes through a bottom-up approach. Specifically, using $ZnCl_2$ and SiO_2 as dual templates and Fe^{2+} as an iron source, SACs with hierarchically porous carbon nanoframe−confined FeN_5 active centers (Fe SAs/N_5-pC-4) were directly synthesized by introducing an excess nitrogen source and employing a polymerization−pyrolysis−evaporation−etching strategy (PPEE). The spatial configuration of the active center of Fe SAs/N_5-pC was verified by theoretical simulation calculations and characterizations. Further, taking oxidase as a model, theoretical calculations and experimental studies have identified the catalytic pathway of Fe SAs/N_5-pC with the participation of O_2. Based on the excellent oxidase-like activity of Fe SAs/N_5-pC, an AChE/acetylthiocholine iodide (ATChI)/Fe SAs/N_5-pC-4 biosensor was successfully constructed and applied to OPs colorimetric analysis.

EXPERIMENTAL SECTION

Preparation of Atomically Dispersed an Fe SAs/N_5-pC Catalyst. Based on the combination of self-made SiO_2 and $ZnCl_2$ as porosity-inducing templates, Fe SAs/N_5-pC was synthesized by a PPEE strategy (Figures 1 and S1). First, SiO_2 was synthesized as the template (Figure S2). Subsequently, a mixture of $FeCl_2·4H_2O$ (0.5 mmol), $ZnCl_2$ (1.0 mmol), 1,10-phenanthroline monohydrate (5 mmol), and SiO_2 (0/1.5/3/4 g) was added to 30 mL of absolute ethanol. Then, the reactants were stirred under reflux at 60 °C overnight. After that, the resulting mixture was rotary-evaporated, dried (60 °C),

https://doi.org/10.1021/acs.analchem.2c02540
Anal. Chem. 2022, 94, 15270−15279

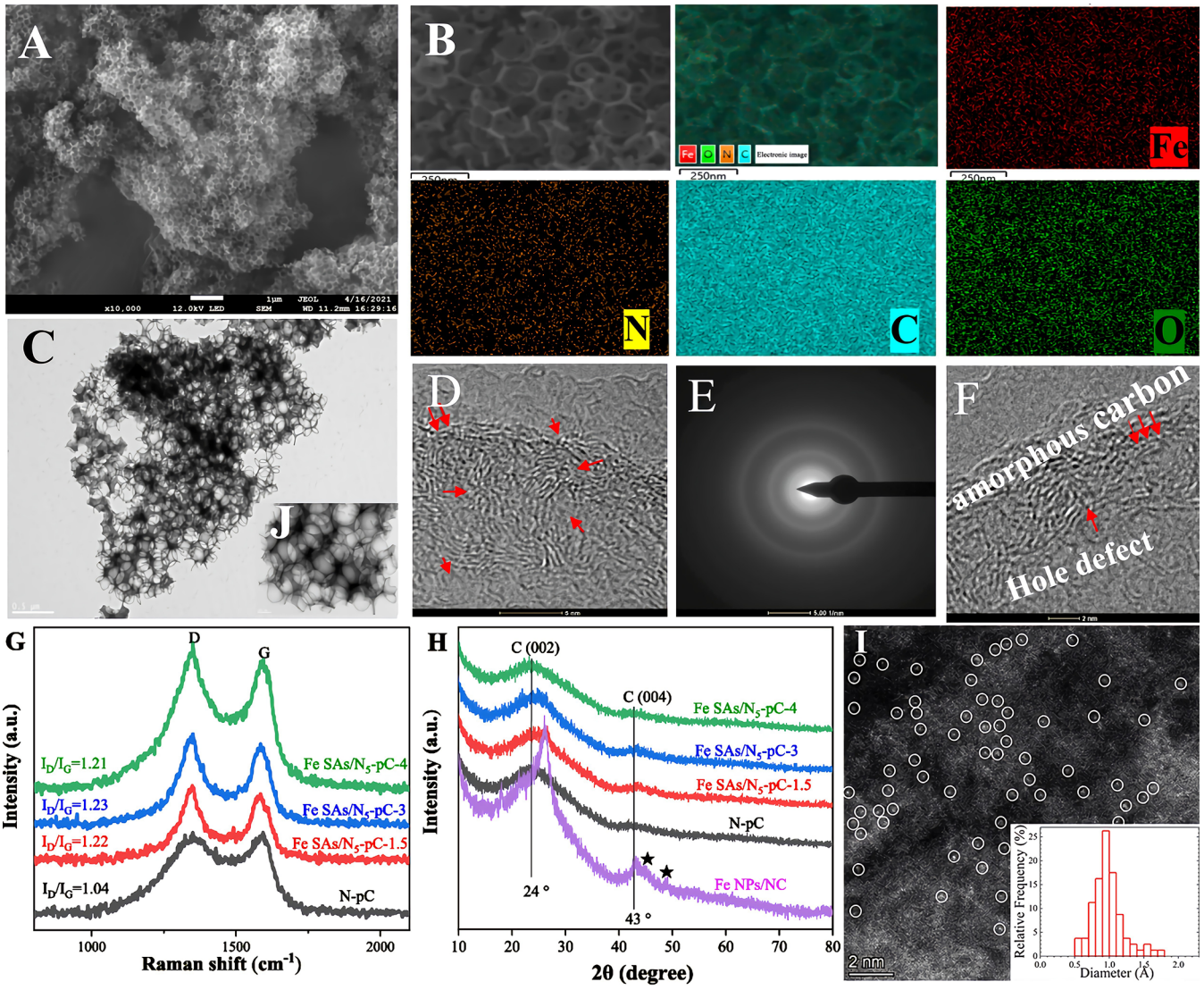

Figure 2. (A) FESEM image, (B) elemental mapping images (Fe, N, C, O), (C) TEM image, (D) HRTEM images, and (E) SAED pattern of Fe SAs/N_5-pC-4. (F) HRTEM images of N-pC. (G) Raman spectra of N-pC and Fe SASs/N_5-pC-*x*. (H) PXRD patterns of N-pC, Fe NPs/NC, and Fe SAs/N_5-pC-*x*. (I) AC-HAADF-STEM images of Fe SAs/N_5-pC-4.

ground, and then heated in a tube furnace using a temperature-programmed method (from 25 to 900 °C at the rate of 5 °C min^{-1} and held for 2 h). The remaining solid was dispersed in 100 mL of 5 wt % HF solution at room temperature for 6 h to remove the SiO_2 template, and this step was repeated 4 times. The resulting black solid is expressed as Fe SAs/N_5-pC-*x* (*x* = 1.5, 3, 4, mass of SiO_2). For comparison, Fe NPs/NC and Fe-N-pC were synthesized via a method similar to Fe SAs/N_5-pC-*x* without the addition of SiO_2 and $ZnCl_2$, respectively, while N-pC was synthesized without the addition of $FeCl_2 \cdot 4H_2O$. The synthesis conditions of each nanozyme are listed in Table S1.

Determination of OP. First, methyl parathion (MP) (40 μL) and AChE solution (20 mU mL^{-1}, 100 μL) were incubated at 37 °C for 5 min to inhibit the activity of AChE. Next, ATChI (1 mM, 60 μL) was added to the above mixture solution and hydrolyzed for 15 min. Then, Fe SAs/N_5-pC (0.3 mg mL^{-1}, 10 μL) was added at room temperature and incubated for 2 min to inhibit the iron-active sites in Fe SAs/N_5-pC. Finally, TMB (1 mM, 100 μL) and HAc-NaAc buffer (pH = 4, 690 μL) were added, and the incubation was continued for 10 min. The absorbance value of the solution at 652 nm was recorded as A_1. The absorbance values at 652 nm in the control experiment without MP and AChE were recorded as A and A_0, respectively. The inhibition rate of AChE activity (I %) was calculated by $I\ \% = \frac{A_1 - A}{A_0 - A} \times 100\%$. The quantitative determination of MP was obtained based on the linear relationship between the MP concentration and the value of inhibition.

Data Analysis and Processing. The processing of the extended X-ray absorption fine structure (EXAFS) data is described in the Supporting Information.

Computational Studies. Density functional theory (DFT) was used to calculate the energetics for the O_2 reduction process of atomically dispersed Fe-N_5 active sites. See the detailed calculation process in the Supporting Information.

RESULTS AND DISCUSSION

Characterization of Fe SAs/N_5-pC. The introduction and etching of SiO_2 endow the synthesized Fe SAs/N_5-pC with a

https://doi.org/10.1021/acs.analchem.2c02540
Anal. Chem. 2022, 94, 15270−15279

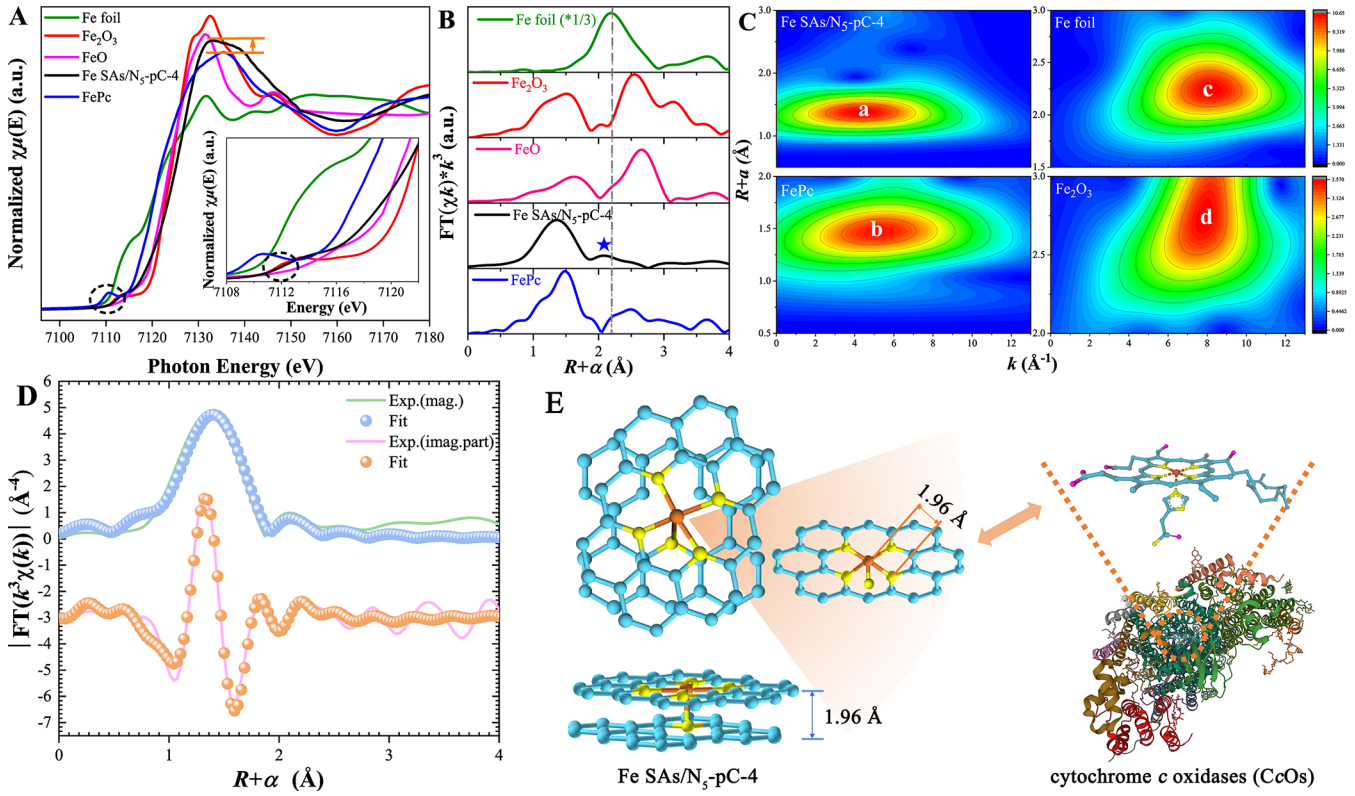

Figure 3. (A) Normalized XANES spectra at the Fe K-edge. (B) Corresponding k^3-weighted FT-EXAFS spectra. (C) WT-EXAFS spectra for Fe SAs/N_5-pC-4. (D) Fe K-edge EXAFS (line) and the curve fit (circle) analysis for Fe SAs/N_5-pC-4 in *R*-space. The data were k^3-weighted and not phase-corrected. (E) Schematic diagram of the structure for Fe SAs/N_5-pC-4. The structural diagram of C*c*Os is from Luo's research.[37]

three-dimensional honeycomb structure, and as the amount of SiO_2 increases, the wall thickness decreases (Figures 2 and S3). This facilitates the kinetic accessibility of available active sites within the reaction time scale.[24] In contrast, Fe nanoparticles appeared in Fe NPs/NC in the absence of SiO_2 support (Figure S4). The added Zn^{2+} acts as a "fence" and further expands the spatial interval between the two Fe atoms. During the carbonization process with continuous nitrogen blowing, the low boiling point zinc atoms (mp 420 °C, bp 907 °C) can be evaporated at a high temperature of 900 °C.[25] The subsequent generation of pyridine nitrogen in carbon nanoframes is beneficial for stabilizing Fe SAs. Meanwhile, the micropores introduced by $ZnCl_2$ are beneficial to provide a larger specific surface area and more active sites.[26] Energy-dispersive X-ray spectroscopy (EDS) mapping (Figure 2B) indicates that Fe, N, C, and O elements are distributed uniformly within Fe SAs/N_5-pC. No metal nanoparticles or clusters were observed in the high-resolution transmission electron microscopy (HRTEM) image of Fe SAs/N_5-pC-4 (Figure 2D), revealing that the iron may be distributed in the N-pC as a single atom. Furthermore, the selected area electron diffraction (SAED) of Fe SAs/N_5-pC-4 appears as a clear amorphous halo structure, which also proves the existence of only a disordered stacked carbon layer and absence of aggregated metal in the material (Figure 2E). In addition, as illustrated in the HRTEM image (Figure 2D,F), the atomic arrangement of N-pC and Fe SAs/N_5-pC-4 is distorted, full of disordered, discontinuous lattice stripes. This can be attributed to the fact that during the annealing process at 900 °C, the atoms at the normal lattice point jump to the interstitial position because of thermal fluctuations. Subsequently, the generated vacancies and interstitial atoms are distorted to form intrinsic defects.

Raman spectroscopy was used to obtain more comprehensive defect structural information of the carbon support. The three Fe SAs/N_5-pC-*x* catalysts exhibited very similar I_D/I_G ratios (1.21−1.23, Figure 2G), indicating that the effect of the carbon framework on the catalytic activity of Fe SAs/N_5-pC-*x* can be excluded, while the focus is to consider the effect of macropores. As shown in Figure S5, the catalytic activity of Fe SAs/N_5-pC-4 is still much higher than that of N-pC even though the Fe sites are shielded by excess SCN^-. This can be attributed to more defects formed after the introduction of Fe (Figure 2G), which improves the mass/electron transfer ability[27] and catalytic efficiency[28] of the nanozyme. In addition, Fe SAs/N_5-pC-*x* presents similar powder X-ray diffraction (PXRD) patterns with N-pC, and two broad peaks at 24° and 43° can be attributable to (002) and (004) crystal planes of carbon. No diffraction peaks corresponding to Fe and its oxides were detected, demonstrating the absence of any large crystalline particles of Fe-containing species in Fe SAs/N_5-pC-*x*. On the contrary, characteristic sharp peaks belonging to Fe_3C in the range of 44−50° were observed for Fe NPs/NC (Figure 2H). The atomically resolved aberration-corrected high-angle annular dark-field scanning transmission electron microscopy (AC-HAADF-STEM) image (Figures 2I and S6) clearly shows that the isolated Fe atoms (0.98 ± 0.26 Å, white dots) are uniformly dispersed on the surface of the carrier, which strongly confirmed the existence of only single Fe atoms. The loading of the Fe element was determined by inductively coupled plasma to be 0.54 weight % (wt %).

https://doi.org/10.1021/acs.analchem.2c02540
Anal. Chem. 2022, 94, 15270−15279

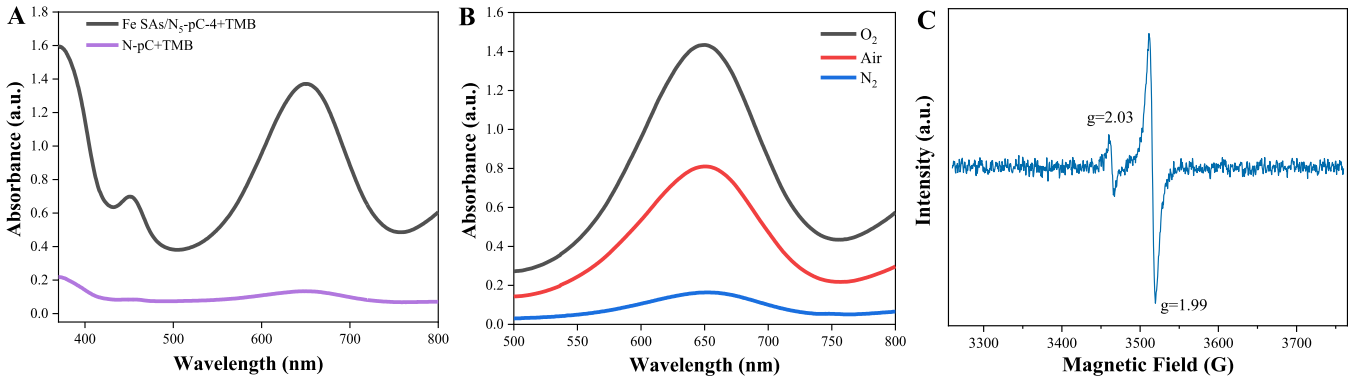

Figure 4. (A) Oxidase-like activity of Fe SAs/N_5-pC-4 (10 μg mL^{-1}) and N-pC (10 μg mL^{-1}). (B) UV−vis absorption spectra of Fe SAs/N_5-pC-4 (3 μg mL^{-1}) in O_2-saturated, air-saturated, and N_2-saturated sodium acetate−acetic acid buffer. (C) X-band EPR spectrum of Fe SAs/N_5-pC-4.

X-ray photoelectron spectroscopy (XPS) and X-ray absorption fine structure (XAFS) data were used to further characterize surface elemental composition and the atomic structures of Fe SAs/N_5-pC-4 (Figures 3 and S7). High-resolution Fe 2p XPS spectra show two peaks at binding energies of 711.9 eV (Fe $2p^{3/2}$) and 724.5 eV (Fe $2p^{1/2}$). These binding energy values and associated oscillatory structures point to Fe^{2+} species.[29] High-resolution N 1s XPS spectra can be further deconvolved into four N species [i.e., pyridinic N (398.7 eV), Fe-N (399.2 eV), graphitic N (401.0 eV), and oxidized N (403.5 eV)] based on the literature methods.[30] Of these, the content of graphite-N (48.3%) is higher than that of pyridine-N (34.8%) due to less stability of pyridine-N at high temperatures (Table S2).[31] XAFS, including X-ray absorption near-edge structure (XANES) and EXAFS, possess high sensitivity for determining the chemical state and coordination information of the absorption center.[32] The XANES curve of Fe SAs/N_5-pC-4 in Figure 3A shows that its near-edge absorption energy is between that of the standard Fe foil and Fe_2O_3 and close to that of FeO. It indicates that the average valence state of Fe is near Fe (II),[14] which is consistent with the XPS results. The pre-edge peak at 7110 eV in the XANES spectrum of iron phthalocyanine (FePc), resulting from the 1s → $4p_z$ transition, was considered as the fingerprint of the square-planar Fe-N_4 coordination with a high D_{4h} symmetry.[33] There is no similar pre-edge peak in Fe SAs/N_5-pC-4, and the white line peak of Fe SAs/N_5-pC-4 is higher than that of FePc. It is shown that Fe SAs/N_5-pC-4 does not exhibit the coordination structure of Fe-N_4, and the coordination number of the first shell of iron is higher than 4.[34] Fe K-edge EXAFS was applied to examine the local coordination information of Fe sites in Fe SAs/N_5-pC-4. In the Fourier-transformed (FT) EXAFS curve (*R*-space) (Figure 3B), a major peak is exhibited at approximately 1.4 Å (without phase correction), close to the first Fe-N shell of the FePc reference. It could be attributed to Fe-N scattering paths.[35] In addition, the three-dimensional information of combined *R* and *k*-space obtained by wavelet transform (WT) of the Fe *k*-edge EXAFS oscillations was used to further verify the coordinated scattering paths of the weak peaks appearing at higher *R* values ($R > 2$ Å, close to the Fe−Fe scattering path).[36] For elements with a higher atomic number, the strongest oscillation in the *k*-space of WT-EXAFS appear at a higher wave number. In the *R* range of 1−3 Å, the k^3-weighted WT-EXAFS spectra for Fe SAs/N_5-pC-4 exhibit one intensity maximum at 4.5 Å^{-1} that was assigned to Fe−N scattering paths. Also, no Fe−Fe scattering paths (compared with Fe foil and Fe_2O_3, 8.0 Å^{-1}) were observed. It proves that the Fe atom existed as a mononuclear center without the presence of Fe-derived crystalline structures (Figure 3C). In conclusion, FT- and WT-EXAFS results confirm that the iron species in Fe SAs/N_5-pC-4 are atomically anchored in the nitrogen-doped hierarchically porous carbon.

Meanwhile, EXAFS fitting analysis was carried out to calculate the first shell coordination atom, coordination number, and interatomic bonding distance of the central Fe sites in Fe SAs/N_5-pC-4. The EXAFS fitting curves are shown in Figures 3D and S8, and the detailed fitting parameters are listed in Table S3. The first coordination shell of Fe SAs/N_5-pC-4 is well-fitted by Fe−N coordination paths with approximately five N atoms, and the average distance between Fe and N atoms is approximately 1.96 Å. This implies that the central Fe sites in Fe SAs/N_5-pC-4 possessed a Fe-N_5 configuration, that is, an in-plane Fe-N_4 moiety with one axial nitrogen atom (Figure 3E).

Oxidase-like Activity Assays. The enzyme-like activity of Fe SAs/N_5-pC-4 was investigated by colorimetry. Fe Sas/N_5-pC-4 possesses highest oxidase-like activity than other nanozymes (Fe Sas/N_5-pC-1.5/3, Fe NPs/NC, Fe-N-pC, and N-pC) (Figure S9). This can be attributed to the hierarchical porous structure (Figure S10), high porosity (87.3%, Table S4), excellent hydrophilicity (Figure S11), and favorable Fe-N_5 coordination of Fe SAs/N_5-pC-4. Furthermore, similar to natural enzymes, the oxidase-like activity of Fe SAs/N_5-pC-4 is also high concentration- and pH-dependent (Figure S12), and the optimal activity was observed at acidic conditions (pH = 4). It is worth noting that Fe SAs/N_5-pC-4 can still maintain at least 70% of the oxidase-like activity even when the test temperature is extended to 60 °C (Figure S13A). Moreover, Fe SAs/N_5-pC-4 showed little change in its oxidase-like activity even after being treated with a strong acid (base) for 24 h (Figure S13B) or on storage at room temperature for 1 year (Figure S13C). The unique stability is the out-performance of the Fe SAs/N_5-pC-4 nanozyme over natural enzymes.

Furthermore, the Michaelis constant (K_M) was measured to quantitatively evaluate the oxidase-like activity of Fe SAs/N_5-pC-4 (Figure S14 and Table S5). Compared with other previously reported nanozymes with oxidase activity, Fe SAs/N_5-pC-4 possesses ultra-high affinity for TMB (lower K_M, 0.116 mM) and better oxidase-like activity (higher K_{cat}/K_M, 3.43 mM^{-1} s^{-1}). Notably, the catalytic rate constant of Fe SAs/N_5-pC-4 (0.398 s^{-1}) is 569 times greater than that of

https://doi.org/10.1021/acs.analchem.2c02540
Anal. Chem. 2022, 94, 15270−15279

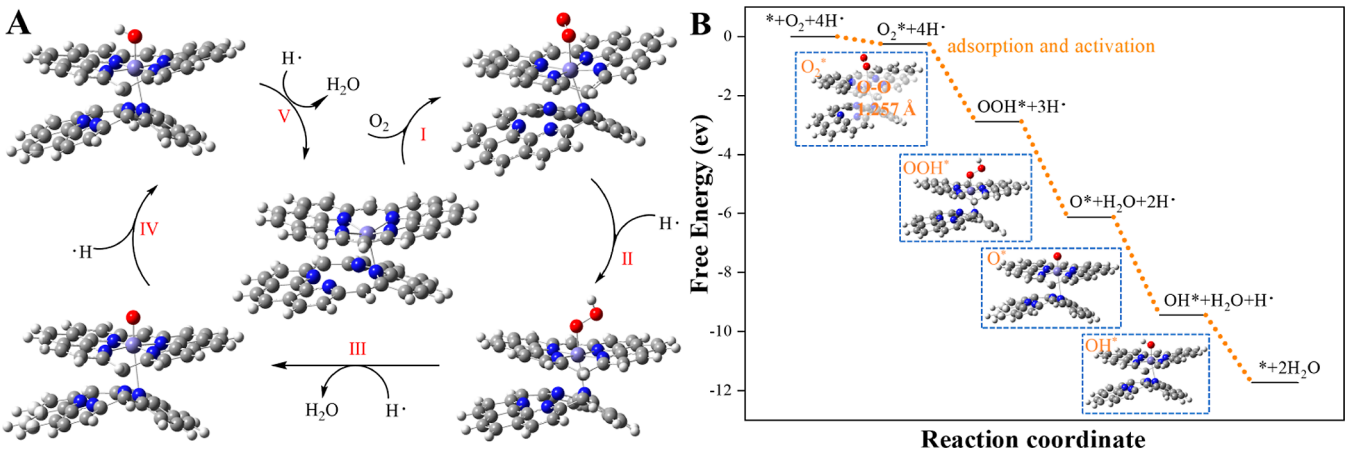

Figure 5. Theoretical investigation on the oxidase-like activity of Fe SAs/N_5-pC-4. (A) Schematic diagram of the elementary step of O_2 reduction to H_2O on Fe SAs/N_5-pC-4. The gray, blue, light blue, red, and white spheres represent C, N, Fe, O, and H atoms, respectively. (B) Free energy diagram for the oxygen reduction reaction on Fe SAs/N_5-pC-4.

commercial Pt/C. In addition, owing to the clear spatial structure of the active site of Fe SAs/N_5-pC-4, it is more conducive to explore the catalytic mechanism than traditional nanozymes. Overall, the Fe SAs/N_5-pC-4 prepared in this study exhibits the advantages of remarkable oxidase-like activity, low cost, and 100% metal atom utilization.

Catalytic Mechanism. The catalytic mechanism of Fe SAs/N_5-pC-4 was further studied through comparative experiments, steady-state kinetic analysis, and electron paramagnetic resonance (EPR). Compared with N-pC, the introduction of Fe significantly enhanced the oxidase-like activity of nanozymes (Figure 4A), suggesting that Fe-N_5 and defects caused by Fe are the main active site in Fe SAs/N_5-pC-4. Under a N_2 atmosphere, TMB could not be oxidized by Fe SAs/N_5-pC-4. Furthermore, the high dependence of Fe SAs/N_5-pC-4 on O_2 in substrate oxidation suggests that it catalyzes the oxidation of substrates while reducing O_2 (Figure 4B). That is, Fe SAs/N_5-pC-4 does not directly act as an oxidant to oxidize TMB. Rather, it does act as an oxidase mimetic, utilizing O_2 to generate reactive species to oxidize TMB.

The reduction of O_2 and the oxidation of substrates are mainly catalyzed by oxidases through the following two pathways.[19]

$$\text{Path one: } A_{red} + O_2 \rightarrow A_{ox} + H_2O_2$$

$$\text{Path two: } A_{red} + O_2 \rightarrow A_{ox} + H_2O$$

First, catalase that can disproportionate H_2O_2 into O_2 and H_2O was added to eliminate possible intermediate H_2O_2, thereby inhibiting the oxidation of TMB. However, the production of oxTMB is hardly affected by catalase (Figure S15), which reveals that H_2O_2 is not an intermediate that plays a key role in the catalytic reaction. Then, the trapping agent 5,5-dimethyl-1-pyrroline N-oxide (DMPO) was used to verify the existence of the superoxide radical ($O_2^{-\bullet}$) or hydroxyl radical ($^\bullet$OH). In Figure S16, there is no observable sixfold signal peak and 1:2:2:1 fourfold signal peak, suggesting that $O_2^{-\bullet}$ and $^\bullet$OH are not the main intermediates of the catalytic reaction. These results confirm that Fe SAs/N_5-pC mediates the complete reduction of molecular oxygen to water without releasing partially reduced oxygen (PROS) (Figure S17). Given this, we propose that the O_2 activation process of Fe SAs/N_5-pC-4 may be similar to that of Ccos, that is, though the path two activates oxygen.[37] The highvalent Fe^{IV}=O species (compounds I) is considered to be a key intermediate in catalytic cycles of many heme iron enzymes and heme analogues.[19] At 77 K, a typical diamond-shaped label signal at $g \approx 2.03$ was detected by EPR, consistent with η^2-peroxo heme species, signifying the formation of Fe^{IV}=O intermediate.[22] This suggests that Fe SAs/N_5-pC-4 may have a similar reaction process with heme analogues.

Theoretical Evaluation on Enzyme-like Activity. To explore the oxidase-like mimetic catalytic mechanisms of Fe SAs/N_5-pC nanozymes, the DFT calculation was proposed to understand the catalytic process at the atomic level (Figure 5).[38] The calculation results imply that the catalytic pathway is based on the free energy change of the following steps (Figure S18)

$$O_2 + {}^* \rightarrow O_2^* \quad (1)$$

$$O_2^* + H^\bullet\,(H^+ + e^-) \rightarrow OOH^* \quad (2)$$

$$OOH^* + H^\bullet\,(H^+ + e^-) \rightarrow O^* + H_2O \quad (3)$$

$$O^* + H^\bullet\,(H^+ + e^-) \rightarrow OH^* \quad (4)$$

$$OH^* + H^\bullet\,(H^+ + e^-) \rightarrow {}^* + H_2O \quad (5)$$

The asterisk (*) represents Fe SAs/N_5-pC-4, and i* represents the active intermediate that is in a state of binding with Fe SAs/N_5-pC-4.

The theoretical distances of atoms for intermediate species are annotated in Figure S19A–G. As shown in Figure 5A, initially, the O_2 molecule would be easily and strongly adsorbed on the top of the Fe-N_5 active site of geometry-optimized Fe SAs/N_5-pC to form an activated ferric-superoxide complex (O_2*) immediately. The O–O distance (1.257 Å, Figure S19B) of O_2* is larger than that of the free O_2 molecule (1.23 Å). It can be attributed to the fact that the electrons on Fe fill the antibonding π* orbital of O_2 under the "electron push effect" of the axial coordination N, thereby weakening the O–O bond.[39] This means that O_2 can be effectively activated on Fe SAs/N_5-pC-4. In addition, under the "push effect", high-spin ($S = 2$) ferrous of Fe SAs/N_5-pC-4 and triplet O_2 combine to form a O_2* with singlet electronic ground states in which low-spin iron centers are antiferro-

https://doi.org/10.1021/acs.analchem.2c02540
Anal. Chem. 2022, 94, 15270−15279

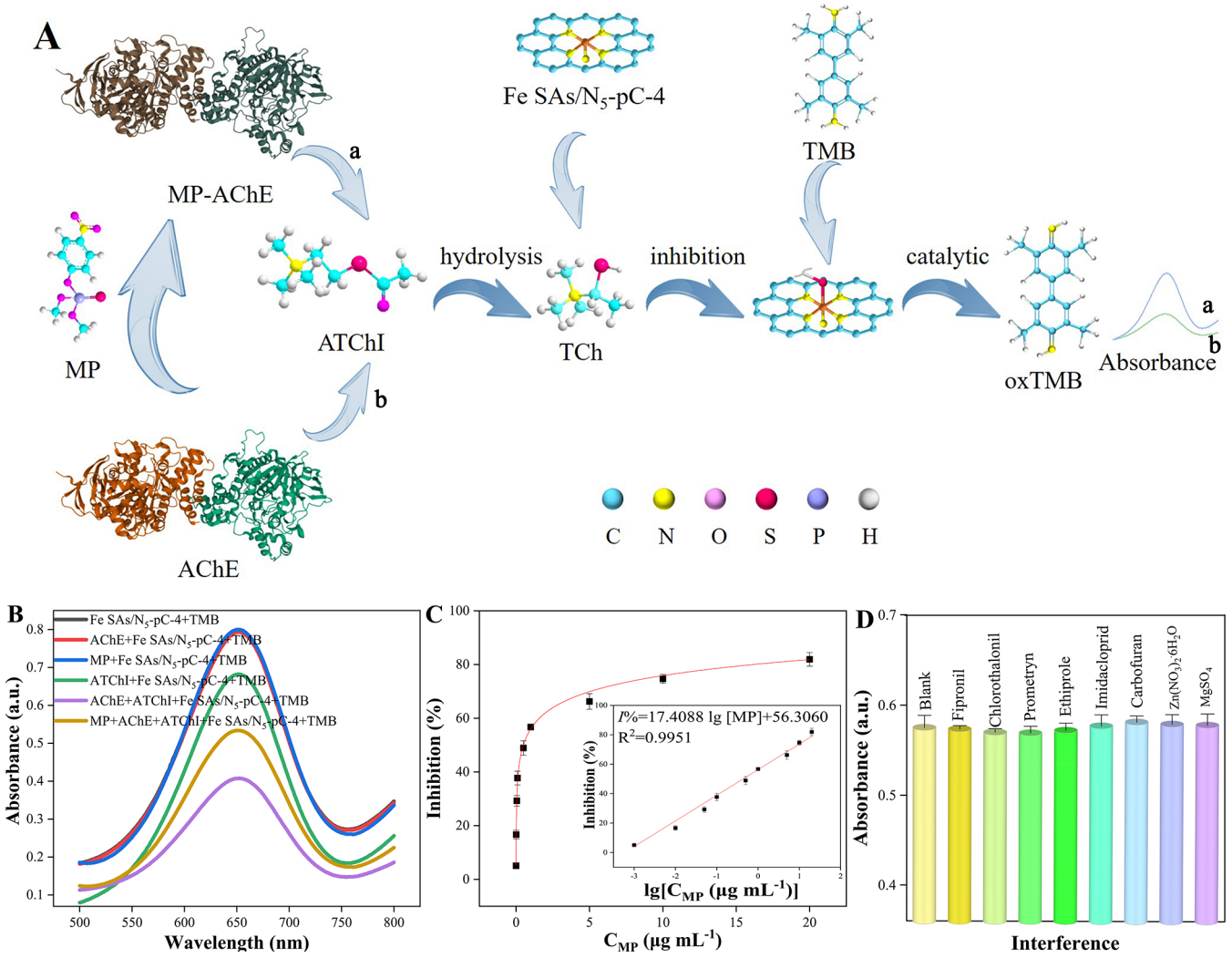

Figure 6. (A) Schematic diagram of the constructed biosensor for determination of OPs. (B) Effect of AChE, MP, ATChI, AChE + ATChI, and MP + AChE + ATChI on the color development of Fe SAs/N_5-pC-4-catalyzed TMB in the biosensor. (C) Relationship between the MP concentration and the inhibition rate of AChE. The inset is the linear relationship between the logarithm of the MP concentration and the inhibition rate of AChE. (D) Effect of different interferences (pesticides and metal ions) in the detection of MP by the biosensor.

magnetically coupled to the doublet superoxide anion.[40] This raises the pK_a of the oxygen atom in the O_2*, facilitating its acquisition of acidic hydrogen from the substrate (TMB) and generation of OOH* with a longer O−O distance (1.450 Å), which leads to both improved activity and selectivity for O_2 reduction to water (Figure S19C,F).[41] Furthermore, along with the snatching of hydrogen species in the TMB by OOH*, a double bond is formed between Fe and O, shortening the Fe−O distance (1.630 Å, Figure S19D,G). Under the "push effect", the Fe^{IV}═O intermediate (O*) generated by dehydration could be better described as a [$N^{\bullet+}$−Fe^{III}−$O^{\bullet-}$] diradical, which can easily further abstract acidic hydrogen from the substrate to form OH* (Figure S19E). Finally, the acidic hydrogen in the substrate approach the OH* to form H_2O molecules and desorb from the surface of Fe SAs/N_5-pC-4, resulting in a significant decrease in the total Gibbs free energy ($\triangle G$ = −2.288 eV). Fe SAs/N_5-pC-4 also returns to the initial state. In the next cycle, the recovered Fe SAs/N_5-pC-4 continuously activates another O_2 molecule. Overall, the DFT results indicate that the Fe SAs/N_5-pC-4 could generate H_2O by activating O_2, thereby exhibiting high oxidase-like activity.

In addition, Fe SAs/N_5-pC-4 also possesses excellent peroxidase-like activity (Figures S20 and S21). However, the experimental and theoretical calculation results show that activation of O_2 is more favorable than activation of H_2O_2 on Fe SAs/N_5-pC from both thermodynamic and kinetic perspectives.

Inhibitory Effect of Sulfhydryl-Containing Small Molecules (−SH). Based on the hard-soft-acid-base theory, the soft end (S) of the two ligands SCN^- can coordinate with the soft acid (Fe (II)) in Fe SAs/N_5-pC-4. As shown in Figure S22A, the oxidase-like activity of Fe SAs/N_5-pC-4 decreases rapidly with the addition of KSCN. The iron in Fe SAs/N_5-pC-4 can also coordinate with thiols through the Fe−S bond, thereby inhibiting its catalytic activity (Figure S22B). The Fourier Transform infrared (FTIR) spectroscopy also confirmed the interaction between Fe SAs/N_5-pC-4 and sulfhydryl-containing small molecules (Figure S22C). New characteristic FTIR peaks appear at 1300−1700 and 3000−3200 cm^{-1} for Fe SAs/N_5-pC-4 inhibited by cysteine (Cys-Fe SAs/N_5-pC-4), indicating the introduction of sulfhydryl-containing molecules. In contrast, the disappearance of the

https://doi.org/10.1021/acs.analchem.2c02540
Anal. Chem. 2022, 94, 15270−15279

sulfhydryl peaks in Cys-Fe SAs/N_5-pC-4 can be attributed to the formation of Fe−S bonds.

OPs Detection Method and Performance Evaluation. Based on the principle of multi-enzyme tandem reaction in organisms and the inhibition of Fe SAs/N_5-pC-4 activity by sulfhydryl groups, an enzyme-linked reaction system was constructed (Figure 6A). Specifically, the substrate ATChI can be hydrolyzed by AChE to produce thiocholine (TCh) small molecules containing sulfhydryl groups that can inhibit the activity of Fe SAs/N_5-pC-4 by forming Fe−S bonds. However, the AChE enzyme activity can be irreversibly inhibited by the formation of phosphorylated AChE with P atoms of OPs. Based on this, a new AChE/ATChI/Fe SAs/N_5-pC-4 biosensor was constructed for the indirect determination of OPs. As shown in Figure 6B, the activity of Fe SAs/N_5-pC-4 was not affected by AChE and MP, but to some extent by ATChI. Under the optimal conditions (Figure S23A−F), the AChE activity decreases with the increased OP amount, resulting in the continuous enhancement of the UV absorption signal at 652 nm. Based on this, the curve of I % and the logarithm of the MP concentration was fitted, and good linearity was obtained in the concentration range of 0.001−20 μg mL^{-1}(Figure 6C). The linear regression equation was estimated to be I % = 17.4088 lg [MP] + 56.3060 (R^2 = 0.9951) with the limit of detection down to 0.0006 μg mL^{-1}. The repeatability and reproducibility were also studied by evaluating the inhibition rate of AChE activity at three MP spiking concentrations (0.05, 0.5, and 10 μg mL^{-1}), and five experiments were repeated at each MP concentration. The relative standard deviation of AChE inhibition (I %) ranged from 2.2 to 6.7% (Table S6). Besides, the influence of coexisting substances (pesticides and metal ions) on the biosensor was investigated. The results in Figure 6D show that the absorption signal at 652 nm does not exceed ±5% deviation in the presence of an interference. Next, the constructed sensor was also successfully used for the detection of other kinds of OPs (phosemet, glyphosate, dipterex, chlorpyrifos, phoxim, tetrachlrvinphose, and acephate) (Figure S24). It can be concluded that the constructed sensor exhibits strong selectivity for OPs, providing a cost-effective method for detecting OPs.

Method Comparison. To highlight the uniqueness of this method, it was compared with some previously reported methods (Table S7) for OP analysis in water samples. Obviously, when compared with other tandem reaction systems, from the point of view of simplicity, sensitivity, linear range, reproducibility, selectivity, and response speed, the proposed biosensor has the potential to become an alternative analytical method for the determination of trace OPs. More importantly, the analysis time of other methods exceeds 50 min, while it does not exceed 32 min for our method. Overall, the constructed AChE/ATChI/Fe SAs/N_5-pC-4 tandem detection system exhibits the advantages of simplicity, rapidity, sensitivity, and accuracy and shows broad potential for rapid and real-time monitoring of OPs in water.

Real Sample Analysis. Furthermore, to challenge the efficacy of the tandem reaction system in a realistic scenario, the determination of MP in actual samples (East Lake water and tap water) was carried out through the standard addition method. The recoveries of MP in spiked tap water and East Lake water samples are in the range of 96−102 and 97−105% (Table S6), respectively. The results confirm the low matrix effect from real water samples and indicate the practical application potential of the tandem reaction system.

CONCLUSIONS

In conclusion, a hierarchically porous carbon-supported SAC with Fe-N_5 active centers was successfully synthesized by a PPEE strategy. Under the electron pushing effect of axial coordination N, O_2 can be efficiently activated by atomically dispersed Fe-N_5 active sites on Fe SAs/N_5-pC-4.Various characterization methods, theoretical simulation calculations, and experiments have proved that Fe SAs/N_5-pC exhibits excellent catalytic behavior, similar to that of natural C*cos*. Notably, the maximized atom utilization efficiency, hierarchical porous structure, excellent hydrophilicity, and axial N-electron-driving mechanism significantly endow Fe SAs/N_5-pC-4 with higher oxidase-like activity compared to other reported oxidases. In particular, the catalytic rate constant of Fe SAs/N_5-pC-4 is 569 times greater than that of commercial Pt/C. Based on the excellent oxidase-like activity and the inhibitory effect of thiols on the active site, a H_2O_2-free AChE/ATChI/Fe SAs/N_5-pC-4 biosensor was constructed and successfully applied to the colorimetric analysis of OPs. The present research results provide ideas for the research and rational design of the catalytic mechanism of SACs. The designed Fe SAs/N_5-pC-4 has the potential to replace traditional nanozymes and provide a huge impetus for the development of novel biosensors.

ASSOCIATED CONTENT

Supporting Information

The Supporting Information is available free of charge at https://pubs.acs.org/doi/10.1021/acs.analchem.2c02540.

Materials, additional experimental details, instrumentation, computational studies, schematic illustration of the nanozymes, FE-SEM, HRTEM, UV−Vis absorption spectra of TMB solutions, AC-HAADF-STEM, XPS spectrum, Fe K-edge EXAFS analysis, oxidase-like activity of different nanozymes, pore size diameter distributions, contact angle, oxidase-like activity of Fe SAs/N_5-pC-4 in different conditions, relative oxidase-like activity of Fe SAs/N_5-pC-4, enzyme kinetics, the effect of catalase on the kinetics of Fe SAs/N_5-pC-4, EPR spectra, schematic illustration of oxidase-like activity of Fe SAs/N_5-pC-4, mechanism for the catalytic oxidation, DFT calculation results, comparison of oxidase-like and peroxidase-like activities, theoretical calculation of peroxidase-like activity, influence of KSCN, schematic diagram of the inhibitory effect of sulfhydryl-containing small molecules, FTIR spectra, performance optimization, detection of different OPs, synthetic conditions, the content of different types of N, curve fit parameters for Fe K-edge EXAFS, various physical quantities obtained by MIP, comparison of the kinetic constants of different nanozymes, analytical performance of the biosensor, and comparison of different biosensors for OP determination (PDF)

AUTHOR INFORMATION

Corresponding Authors

Hui Xu − *Key Laboratory of Insecticide & Chemical Biology, Ministry of Education, College of Chemistry, Central China*

https://doi.org/10.1021/acs.analchem.2c02540
Anal. Chem. 2022, 94, 15270−15279

Normal University, Wuhan 430079, China; orcid.org/0000-0003-1999-9806; Email: huixu@ccnu.edu.cn

Ganbing Zhang − *College of Chemistry and Chemical Engineering, Hubei University, Wuhan 430062, China;* Email: gbzhang@hubu.edu.cn

Authors

Tiantian Chen − *Key Laboratory of Insecticide & Chemical Biology, Ministry of Education, College of Chemistry, Central China Normal University, Wuhan 430079, China*

Dandan Zhou − *Key Laboratory of Insecticide & Chemical Biology, Ministry of Education, College of Chemistry, Central China Normal University, Wuhan 430079, China*

Shenghuai Hou − *Key Laboratory of Insecticide & Chemical Biology, Ministry of Education, College of Chemistry, Central China Normal University, Wuhan 430079, China*

Yan Li − *Key Laboratory of Insecticide & Chemical Biology, Ministry of Education, College of Chemistry, Central China Normal University, Wuhan 430079, China*

Ying Liu − *Key Laboratory of Insecticide & Chemical Biology, Ministry of Education, College of Chemistry, Central China Normal University, Wuhan 430079, China*

Manlin Zhang − *Key Laboratory of Insecticide & Chemical Biology, Ministry of Education, College of Chemistry, Central China Normal University, Wuhan 430079, China*

Complete contact information is available at: https://pubs.acs.org/10.1021/acs.analchem.2c02540

Author Contributions

The manuscript was written through contributions of all authors. All authors have given approval to the final version of the manuscript.

Notes

The authors declare no competing financial interest.

■ ACKNOWLEDGMENTS

This research was financially supported by the National Natural Science Foundation of China (no. 22076059), International Joint Research Center for Intelligent Biosensing Technology and Health, and the 111 Project B17019.

■ REFERENCES

(1) Lu, C.; Barr, D. B.; Pearson, M. A.; Waller, L. A. *Environ. Health Perspect.* **2008**, *116*, 537−542.
(2) Nasiri, M.; Ahmadzadeh, H.; Amiri, A. *Talanta* **2021**, *227*, 122078.
(3) Wan, M.; Xiang, F.; Liu, Z.; Guan, D.; Shao, Y.; Zheng, L.; Jin, M.; She, Y.; Cao, L.; Jin, F.; Chen, R.; Wang, S.; Wu, Y.; Abd El-Aty, A. M. A.; Wang, J. *Food Chem.* **2021**, *365*, 130485.
(4) Marinov, I.; Ivanov, Y.; Vassileva, N.; Godjevargova, T. *Sens. Actuators, B* **2011**, *160*, 1098−1105.
(5) Zhu, Y.; Wu, J.; Han, L.; Wang, X.; Li, W.; Guo, H.; Wei, H. *Anal. Chem.* **2020**, *92*, 7444−7452.
(6) Liang, M.; Fan, K.; Pan, Y.; Jiang, H.; Wang, F.; Yang, D.; Lu, D.; Feng, J.; Zhao, J.; Yang, L.; Yan, X. *Anal. Chem.* **2013**, *85*, 308−312.
(7) Arduini, F.; Forchielli, M.; Amine, A.; Neagu, D.; Cacciotti, I.; Nanni, F.; Moscone, D.; Palleschi, G. *Microchim. Acta* **2015**, *182*, 643−651.
(8) Wu, J.; Wang, X.; Wang, Q.; Lou, Z.; Li, S.; Zhu, Y.; Qin, L.; Wei, H. *Chem. Soc. Rev.* **2019**, *48*, 1004−1076.
(9) Li, S.; Zhang, Y.; Wang, Q.; Lin, A.; Wei, H. *Anal. Chem.* **2022**, *94*, 312−323.
(10) Singh, N.; Mugesh, G. *Angew. Chem.* **2019**, *131*, 7879−7883.
(11) Wang, X.; Gao, X. J.; Qin, L.; Wang, C.; Song, L.; Zhou, Y. N.; Zhu, G.; Cao, W.; Lin, S.; Zhou, L.; Wang, K.; Zhang, H.; Jin, Z.; Wang, P.; Gao, X.; Wei, H. *Nat. Commun.* **2019**, *10*, 704.
(12) Xi, Z.; Cheng, X.; Gao, Z.; Wang, M.; Cai, T.; Muzzio, M.; Davidson, E.; Chen, O.; Jung, Y.; Sun, S.; Xu, Y.; Xia, X. *Nano Lett.* **2020**, *20*, 272−277.
(13) Hu, Y.; Gao, X. J.; Zhu, Y.; Muhammad, F.; Tan, S.; Cao, W.; Lin, S.; Jin, Z.; Gao, X.; Wei, H. *Chem. Mater.* **2018**, *30*, 6431−6439.
(14) Wang, Q.; Yang, Y.; Sun, F.; Chen, G.; Wang, J.; Peng, L.; Chen, W. T.; Shang, L.; Zhao, J.; Sun-Waterhouse, D.; Zhang, T.; Waterhouse, G. I. N. *Adv. Energy Mater.* **2021**, *11*, 2100219.
(15) Yang, X. F.; Wang, A. Q.; Qiao, B. T.; Li, J.; Liu, J. Y.; Zhang, T. *Acc. Chem. Res.* **2013**, *46*, 1740−1748.
(16) Wu, Y.; Wu, J.; Jiao, L.; Xu, W.; Wang, H.; Wei, X.; Gu, W.; Ren, G.; Zhang, N.; Zhang, Q.; Huang, L.; Gu, L.; Zhu, C. *Anal. Chem.* **2020**, *92*, 3373−3379.
(17) He, L.; Jiang, Z. W.; Li, W.; Li, C. M.; Huang, C. Z.; Li, Y. F. *ACS Appl. Mater. Interfaces* **2018**, *10*, 28868−28876.
(18) Wu, J.; Yang, Q.; Li, Q.; Li, H.; Li, F. *Anal. Chem.* **2021**, *93*, 4084−4091.
(19) Huang, X.; Groves, J. T. *Chem. Rev.* **2018**, *118*, 2491−2553.
(20) Chatterjee, S.; Sengupta, K.; Samanta, S.; Das, P. K.; Dey, A. *Inorg. Chem.* **2015**, *54*, 2383−2392.
(21) Xie, L.; Zhang, X. P.; Zhao, B.; Li, P.; Qi, J.; Guo, X.; Wang, B.; Lei, H.; Zhang, W.; Apfel, U. P.; Cao, R. *Angew. Chem., Int. Ed. Engl.* **2021**, *60*, 7576−7581.
(22) Huang, L.; Chen, J.; Gan, L.; Wang, J.; Dong, S. *Sci. Adv.* **2019**, *5*, No. eaav5490.
(23) Xu, W.; Song, W.; Kang, Y.; Jiao, L.; Wu, Y.; Chen, Y.; Cai, X.; Zheng, L.; Gu, W.; Zhu, C. *Anal. Chem.* **2021**, *93*, 12758−12766.
(24) Lee, S. H.; Kim, J.; Chung, D. Y.; Yoo, J. M.; Lee, H. S.; Kim, M. J.; Mun, B. S.; Kwon, S. G.; Sung, Y. E.; Hyeon, T. *J. Am. Chem. Soc.* **2019**, *141*, 2035−2045.
(25) Yin, P.; Yao, T.; Wu, Y.; Zheng, L.; Lin, Y.; Liu, W.; Ju, H.; Zhu, J.; Hong, X.; Deng, Z.; Zhou, G.; Wei, S.; Li, Y. *Angew. Chem.* **2016**, *128*, 10958−10963.
(26) Zhao, X.; Zhao, H.; Zhang, T.; Yan, X.; Yuan, Y.; Zhang, H.; Zhao, H.; Zhang, D.; Zhu, G.; Yao, X. *J. Mater. Chem. A* **2014**, *2*, 11666−11671.
(27) Zhu, C.; Li, H.; Fu, S.; Du, D.; Lin, Y. *Chem. Soc. Rev.* **2016**, *45*, 517−531.
(28) Xue, Y.; Huang, B.; Yi, Y.; Guo, Y.; Zuo, Z.; Li, Y.; Jia, Z.; Liu, H.; Li, Y. *Nat. Commun.* **2018**, *9*, 1460.
(29) Xu, X.; Tang, J.; Kaneti, Y. V.; Tan, H.; Chen, T.; Pan, L.; Yang, T.; Bando, Y.; Yamauchi, Y. *Mater. Sci.* **2020**, *7*, 1404−1412.
(30) Wei, X.; Luo, X.; Wang, H.; Gu, W.; Cai, W.; Lin, Y.; Zhu, C. *Appl. Catal., B* **2020**, *263*, 118347.
(31) Wu, J.; Ma, L.; Yadav, R. M.; Yang, Y.; Zhang, X.; Vajtai, R.; Lou, J.; Ajayan, P. M. *ACS Appl. Mater. Interfaces* **2015**, *7*, 14763−14769.
(32) Fei, H.; et al. *Nat. Catal.* **2018**, *1*, 63−72.
(33) Zitolo, A.; Goellner, V.; Armel, V.; Sougrati, M. T.; Mineva, T.; Stievano, L.; Fonda, E.; Jaouen, F. *Nat. Mater.* **2015**, *14*, 937−942.
(34) Qian, K.; Chen, H.; Li, W.; Ao, Z.; Wu, Y. N.; Guan, X. *Environ. Sci. Technol.* **2021**, *55*, 7034−7043.
(35) Tan, H.; Tang, J.; Henzie, J.; Li, Y.; Xu, X.; Chen, T.; Wang, Z.; Wang, J.; Ide, Y.; Bando, Y.; Yamauchi, Y. *ACS Nano* **2018**, *12*, 5674−5683.
(36) Funke, H.; Scheinost, A. C.; Chukalina, M. *Phys. Rev. B: Condens. Matter Mater. Phys.* **2005**, *71*, 094110.
(37) Luo, F.; Shinzawa-Itoh, K.; Hagimoto, K.; Shimada, A.; Shimada, S.; Yamashita, E.; Yoshikawa, S.; Tsukihara, T. *Acta Crystallogr., Sect. F: Struct. Biol. Cryst. Commun.* **2018**, *74*, 92−98.
(38) Shen, X.; Liu, W.; Gao, X.; Lu, Z.; Wu, X.; Gao, X. *J. Am. Chem. Soc.* **2015**, *137*, 15882−15891.
(39) Chatterjee, S.; Sengupta, K.; Samanta, S.; Das, P. K.; Dey, A. *Inorg. Chem.* **2015**, *54*, 2383−2392.
(40) Weiss, J. J. *Nature* **1964**, *202*, 83−84.

(41) Xie, L.; Zhang, X. P.; Zhao, B.; Li, P.; Qi, J.; Guo, X.; Wang, B.; Lei, H.; Zhang, W.; Apfel, U. P.; Cao, R. *Angew. Chem., Int. Ed.* **2021**, *60*, 7576−7581.

https://doi.org/10.1021/acs.analchem.2c02540
Anal. Chem. 2022, 94, 15270−15279